Fully relativistic implicit particle-in-cell simulation scheme

Koichi Noguchi

Physics and Astronomy Department, Rice University,

6100 Main Street, Houston, TX 77005

Cesare Tronci

Imperial College London, Mathematics Department, United Kingdom and

Tera Foundation, Novara, Italy

Gianluca Zuccaro

Plasma Theory Group, Theoretical Division, Los Alamos National Laboratory,

Mail Stop: K717, Los Alamos, NM 87545 and

DISMIC, Politecnico di Torino, Corso Duca degli Abruzzi 10129, Torino, Italy

Giovanni Lapenta*

Centre for Plasma Astrophysics, Departement Wiskunde,

Katholieke Universiteit Leuven, Heverlee, Belgium and

Plasma Theory Group, Theoretical Division,

Los Alamos National Laboratory, Mail Stop: K717, Los Alamos, NM 87545

(Dated: December 15, 2006)

Abstract

We formulate the relativistic implicit time-dependent Vlasov-Maxwell's system based on the simplified implicit Maxwell solver. An implicit finite difference algorithm is developed to solve the Maxwell's equations and equations of motion without coupling to each other, and is implemented to a newly developed 1d3v code. We test the code against the two stream instability, ion acoustic wave damping, Weibel instability and Poynting flux acceleration, and numerical results are all in agreement with analytical solutions.

*Electronic address: lapenta@lanl.gov

I. INTRODUCTION

The complexities of plasma phenomena come from multiscale coupling in space and time. The macroscopic evolution of the system often is developed in relatively slow, but is tightly coupled with smaller and faster scale phenomena. For instance, the topological changes of magnetic field configuration in large scale are not possible without dissipations in small scales. There are two major approaches for simulating plasma: fluid and kinetic [1].

On the one hand, fluid approaches can cover the overall system scales, but are not completely consistent because of spatial averaging which requires information from microscopic kinetic models to deal with the coupling between micro- and macroscopic scales. On the other hand, kinetic approaches are most suitable for the microscopic scales, but extremely costly to extend to full system scales. In order to fill the gap between these approaches, new algorithms are employed in modern space and fusion research. In space plasma physics, global hybrid (fluid electrons and kinetic ions) simulations are done in the large scale problems in the Earth's magnetosphere [1, 2], and gyrokinetic transport simulations in fusion devices are extensively developed [3, 4].

However, hybrid and gyrokinetic models have some crucial limitations. Hybrid models are based on fluid electrons, and processes based on microscopic electron physics, such as electron acceleration, heating, resistivity and viscosity, are not properly described. Hybrid models rely on the continuum and quasineutrality assumptions, which removes the fastest (Langmuir) waves and smallest (Debye) scales. The results can be unphysical when these assumptions fail, unless one provide proper models of high order moments such as the pressure tensor and heat flux [5]. Charge separation can also affect large scale behaviors in reconnection process [6, 7].

Gyrokinetic models are based on averaging the kinetic equations over the gyroperiod of the plasma species [3], which restricts the spatial resolution by $\rho_s/L_{eq} \ll 1$ and time resolution by $\tau\omega cs \ll 1$. Here, L_{eq} and τ are the typical spatial and time scales of equilibrium, and ρ_s and ω_{cs} are the gyroradius and the cyclotron frequency of species s, respectively. Small scales such as Debye length are also typically eliminated by the averaging, and no coupling with gyromotion is allowed.

The gyrokinetic approach is valid in most current experimental fusion devices where the electron and ion gyroradii are much smaller than the scale of interest. However, in any

future thermonuclear burning experiment such as ITER, the assumptions for the gyrokinetic approaches may fail for alpha particles generated by fusion. The gyroradius of alpha particles at 3.5 MeV is of the order of 10cm, which may be too large to allow a gyroaveraging, while electrons and ions still can be treated with the gyrokinetic approach.

Here we employ a fully kinetic approach without gyroaveraging nor quasineutrality assumption. The implicit particle in cell (PIC) method was developed based on a fully kinetic approach that did not rely on any physical approximation but only on the use of advanced numerical methods to reduce the computational cost of large scale simulations. The most simplest PIC method uses explicit numerical techniques requiring to resolve the smallest spatial (Debye) and time (Langmuir frequency) scales [8]. However, the implicit PIC method do not eliminate the smallest scales but keep them in a approximate inexact way sustaining the coupling with larger scales [11].

The implicit PIC method has been developed for many years, including the development and applications of CELESTE3D [9]. However, the extension to treat relativistic systems has never discussed because of non-linearity of the relativistic equation of motion. Here, we propose for the first time the relativistic implicit PIC algorithm, which does not require iterations between the Maxwell's equations and particles per each computational cycle.

We report two new particle movers using a predictor-corrector and Newton-Krylov methods, and a new field solver. These new algorithm is implemented to a newly developed 1D code, and its performance is tested against four problems: the two stream instability (TSI), ion acoustic wave damping (IAW), Weibel instability and Poynting flux acceleration (PFA).

The paper is organized as follows. Section II describes the relativistic implicit scheme, including two algorithms for the particle mover and the field solver. Section III discusses four benchmark problems validating and vefificating the new 1D code. Section IV summarizes the relativistic algorithm and the performances of the 1D code.

II. RELATIVISTIC MOMENT IMPLICIT PIC

A. Maxwell's equations

Following Refs. [9] and [10], we consider Maxwell's equations:

$$\begin{aligned} \nabla \times \boldsymbol{E} + \frac{\partial \boldsymbol{B}}{\partial t} &= 0, \\ \nabla \times \boldsymbol{B} - \frac{1}{c^2}\frac{\partial \boldsymbol{E}}{\partial t} &= \mu_0 \boldsymbol{J}, \\ \nabla \cdot \boldsymbol{E} &= \frac{\rho}{\epsilon_0}, \\ \nabla \cdot \boldsymbol{B} &= 0, \end{aligned} \tag{1}$$

and the Vlasov equation for the distribution function $f_s(\boldsymbol{x}, \boldsymbol{p}, t)$ in phase space for each species s:

$$\frac{\partial f_s}{\partial t} + \frac{\boldsymbol{p}}{m_s} \cdot \frac{\partial f_s}{\partial \boldsymbol{x}} + q_s \left(\boldsymbol{E} + \frac{\boldsymbol{p}}{m_s \gamma} \times \boldsymbol{B} \right) \cdot \frac{\partial f_s}{\partial \boldsymbol{p}} = 0, \tag{2}$$

where $\boldsymbol{x}$ and $\boldsymbol{p}$ are position and momentum, and $\gamma = \sqrt{1 + p^2/(m_s c)^2}$, respectively.

As the fundamental assumption of the particle-in-cell method, we further assume that the distribution function f_s can be described by a superposition of N_s superparticles labeled by p as

$$f_s(\boldsymbol{x}, \boldsymbol{p}, t) = \sum_{p=1}^{Ns} S(x - x_p) S(y - y_p) S(z - z_p) \delta(\boldsymbol{p} - \boldsymbol{p}_p), \tag{3}$$

where S is the shape function, N_s is the total number of particles in the system, and δ is Dirac's delta. We define the shape function as $S(x - x_p) = b_0[(x - x_p)/\Delta x]$, where Δx is a particle and cell size, and b_0 is the b spline of order 0:

$$b_1(\xi) = \begin{cases} 1 \text{ if } \quad |\xi| < 1 \\ 0 \text{ otherwise} \end{cases} . \tag{4}$$

The linearity of the definition in Eq. (3) ensures that the evolution of each superparticle is still described by the Vlasov equation (2). The equations for the evolution of the parameters $\boldsymbol{x}_p$ and $\boldsymbol{u}_p = \boldsymbol{p}_p/m_s$ can be derived by substituting Eq. (3) into Eq. (2), which yields

$$\frac{d\boldsymbol{x}_p}{dt} = \frac{\boldsymbol{u}_p}{\gamma_p}, \tag{5}$$

$$\frac{d\boldsymbol{u}_p}{dt} = \boldsymbol{f}_p, \tag{6}$$

where the average force acting on the finite-sized superparticle $\boldsymbol{f}_p$ is defined as

$$\boldsymbol{f}_p = q_p(\boldsymbol{E}_p + \frac{\boldsymbol{u}_p}{\gamma_p} \times \boldsymbol{B}_p). \tag{7}$$

Here, the average field acting on the superparticle can be described as

$$\boldsymbol{E}_p = \int_V \boldsymbol{E}(\boldsymbol{x}) S(\boldsymbol{x} - \boldsymbol{x}_p) d\boldsymbol{x} = \sum_g \boldsymbol{E}_g W(\boldsymbol{x} - \boldsymbol{x}_p), \tag{8}$$

$$\boldsymbol{B}_p = \int_V \boldsymbol{B}(\boldsymbol{x}) S(\boldsymbol{x} - \boldsymbol{x}_p) d\boldsymbol{x} = \sum_g \boldsymbol{B}_g W(\boldsymbol{x} - \boldsymbol{x}_p), \tag{9}$$

where V is the computational domain, $W(x - x_p) = b_1(x - x_p)/\Delta x$, and the field values in the cell g are given by $\boldsymbol{E}_g$ and $\boldsymbol{B}_g$ (see Lapenta et al. [9] for more detailed discussion.) Here, b_1 is the b spline of order 1,

$$b_1(\xi) = \begin{cases} 1 - |\xi| & \text{if} \quad |\xi| < 1 \\ 0 & \text{otherwise} \end{cases}. \tag{10}$$

Similarly, the charge density ρ and current J for the species s on the grid g can be calculated easily by the summation of the superparticles

$$\rho_{s,g} = \sum_{p=1}^{Ns} q_p W(\boldsymbol{x} - \boldsymbol{x}_p), \tag{11}$$

$$\boldsymbol{J}_{s,g} = \sum_{p=1}^{Ns} q_p \frac{\boldsymbol{u}_p}{\gamma_p} W(\boldsymbol{x} - \boldsymbol{x}_p). \tag{12}$$

Next, we discretize the time domain. The solution is advanced with discrete time interval Δt from the initial time $t^0 = 0$ to the last time $t^N = T$. The generic quantity Ψ at timestep $n(t = t^n)$ is denoted by Ψ^n.

Temporal discretized Maxwell's equations (1) can be written as

$$\nabla \times \boldsymbol{E}^{n+\theta} + \frac{\boldsymbol{B}^{n+1} - \boldsymbol{B}^n}{\Delta t} = 0, \tag{13}$$

$$\nabla \times \boldsymbol{B}^{n+\theta} - \frac{1}{c^2} \frac{\boldsymbol{E}^{n+1} - \boldsymbol{E}^n}{\Delta t} = \mu_0 \boldsymbol{J}^{n+1/2}, \tag{14}$$

$$\nabla \cdot \boldsymbol{E}^{n+\theta} = \frac{\rho^{n+\theta}}{\epsilon_0}, \tag{15}$$

$$\nabla \cdot \boldsymbol{B}^n = \nabla \cdot \boldsymbol{B}^{n+1} = 0. \tag{16}$$

The parameter $\theta \in [1/2, 1]$ is chosen to adjust the numerical dispersion relation for electromagnetic waves. For $\theta = 1/2$, the scheme is second-order accurate in Δt, and for $1/2 < \theta \leq 1$ the scheme is first-order accurate, the same as the classical method [9, 11].

The key to the implicit moment method formulation is to derive suitable set of moment equations that can approximate the particle motion over a computational cycle. The field sources $\rho^{n+\theta}$ and $\boldsymbol{J}^{n+1/2}$ has to be computed directly using particle information only from the previous computational cycle in order to avoid the expensive iteration procedures between the particle and field equations.

The approach we apply here in this implicit moment method is based on a series expansion of the interpolation function W appearing in the expression for the field sources, Eqs. (11) and (12) [10, 11]. The expansion is done with respect to the particle position, choosing the center of the expansion as the particle position at $t = n$:

$$W(\boldsymbol{x}-\boldsymbol{x}_p^{n+1}) = W(\boldsymbol{x}-\boldsymbol{x}_p^n)+(\boldsymbol{x}-\boldsymbol{x}_p^n)\cdot\nabla W(\boldsymbol{x}-\boldsymbol{x}_p^n)+\frac{1}{2}(\boldsymbol{x}-\boldsymbol{x}_p^n)(\boldsymbol{x}-\boldsymbol{x}_p^n):\nabla\nabla W(\boldsymbol{x}-\boldsymbol{x}_p^n)+\cdots, \tag{17}$$

where a tensor notation is used. Performing a Taylor expansion to second order in $\boldsymbol{x} - \boldsymbol{x}_p^n$ on the Eq. (11), we have

$$\begin{aligned}
\rho^{n+1/2}(\boldsymbol{x}) &= \sum_{p=1}^{Ns} q_p W(\boldsymbol{x} - \boldsymbol{x}_p^{n+1/2}) \\
&\simeq \sum_{p=1}^{Ns} q_p \left[W(\boldsymbol{x} - \boldsymbol{x}_p^n) - (\boldsymbol{x}_p^{n+1/2} - \boldsymbol{x}_p^n)\cdot\nabla W(\boldsymbol{x} - \boldsymbol{x}_p^{n+1/2}) \right. \\
&\quad \left. - \frac{1}{2}(\boldsymbol{x}_p^{n+1/2} - \boldsymbol{x}_p^n)(\boldsymbol{x}_p^{n+1/2} - \boldsymbol{x}_p^n) : \nabla\nabla W(\boldsymbol{x} - \boldsymbol{x}_p^n) + \cdots \right].
\end{aligned} \tag{18}$$

Each successive term is higher order in the average excursion of a particle in configuration space in a time step. If this excursion is less than the linear dimension of a finite-size particle, the series converges.

Now we want to replace the term $\boldsymbol{x}_p^{n+1/2} - \boldsymbol{x}_p^n$ by the average velocity $\bar{\boldsymbol{v}}_p$ derived from the equations of motion. The equations of motion are discretized as

$$\boldsymbol{x}_p^{n+1} = \bar{\boldsymbol{v}}_p \Delta t, \tag{19}$$

$$\boldsymbol{u}_p^{n+1} = \boldsymbol{u}_p^n + \frac{q_s \Delta t}{m_s}\left(\boldsymbol{E}_p^{n+\theta}(\boldsymbol{x}_p^{n+1/2}) + \bar{\boldsymbol{v}}_p \times \boldsymbol{B}_p^n(\boldsymbol{x}_p^{n+1/2})\right), \tag{20}$$

where the average velocity $\bar{\boldsymbol{v}}_p$ is defined as

$$\bar{\boldsymbol{v}}_p = \frac{\boldsymbol{u}_p^{n+1} + \boldsymbol{u}_p^n}{\gamma_p^{n+1} + \gamma_p^n}. \tag{21}$$

Substituting Eq. (21) into Eq. (20) yields

$$(\gamma_p^{n+1} + \gamma_p^n)\bar{\boldsymbol{v}}_p - 2\boldsymbol{u}_p^n = 2\beta_s\left(\boldsymbol{E}_p^{n+\theta}(\boldsymbol{x}_p^{n+1/2}) + \bar{\boldsymbol{v}}_p \times \boldsymbol{B}_p^n(\boldsymbol{x}_p^{n+1/2})\right), \tag{22}$$

where $\beta_s = q_s \Delta t/(2m_s)$ which is unique to a given species.

Since $\gamma_p^n = \sqrt{1+(u_p^n/c)^2}$, the inner product of Eq. (20) and $\bar{\boldsymbol{v}}$ becomes

$$\Delta\gamma_p = \gamma_p^{n+1} - \gamma_p^n = \frac{2\beta_s}{c^2}\boldsymbol{E}_p^{n+\theta}(\boldsymbol{x}_p^{n+1/2}) \cdot \bar{\boldsymbol{v}}_p \tag{23}$$

Finally, substituting Eq. (23) into Eq. (22), we have

$$\left(\frac{2\beta_s}{c^2}\boldsymbol{E}_p^n(\boldsymbol{x}_p^n)\cdot\boldsymbol{v}_p^n + 2\gamma_p^n\right)\bar{\boldsymbol{v}}_p - 2\boldsymbol{u}_p^n = 2\beta_s\left(\boldsymbol{E}_p^{n+\theta}(\boldsymbol{x}_p^{n+1/2}) + \bar{\boldsymbol{v}}_p \times \boldsymbol{B}_p^{n+\theta}(\boldsymbol{x}_p^{n+1/2})\right). \tag{24}$$

Note that we keep only the leading order terms of Eq. (23) in Eq. (24) by assuming the relativistic correction term $\Delta\gamma_p$ is small ($\Delta\gamma_p \ll \gamma_n$). We also mention here that this collection term vanishes in the classical limit ($c \gg 1$).

For convenience, we introduce hat quantities $\widehat{\Psi}$ by explicit transform of known quantities from the previous computational cycle. The velocity equation (24) is recast into the following form:

$$\bar{\boldsymbol{v}}_p = \widehat{\boldsymbol{v}}_p + \beta_p' \widehat{\boldsymbol{E}}_p^{n+\theta}(\boldsymbol{x}_p^{n+1/2}), \tag{25}$$

where

$$\widehat{\boldsymbol{v}}_p = \boldsymbol{\alpha}_p^n \cdot (\gamma_p^n \boldsymbol{v}_p^n) \tag{26}$$

$$\widehat{\boldsymbol{E}}_p^{n+\theta} = \boldsymbol{\alpha}_p^n \cdot \boldsymbol{E}_p^{n+\theta}. \tag{27}$$

The transformation tensor operators $\boldsymbol{\alpha}_p^n$ are defined as

$$\boldsymbol{\alpha}_p^n = \frac{1}{D_p^n}\left(\boldsymbol{I} - \beta_p'\boldsymbol{I}\times\boldsymbol{B}_p^n + \beta_p'^2\boldsymbol{B}_p^n\boldsymbol{B}_p^n\right) \tag{28}$$

where

$$\beta_p' = \frac{\beta_s}{\Gamma_p}, \tag{29}$$

$$D_p^n = \Gamma_p\left[1 + (\beta_p' B_p^n)^2\right], \tag{30}$$

$$\Gamma_p = \frac{\beta}{c^2}\boldsymbol{E}_p^n \cdot \boldsymbol{v}_p^n + \gamma_p^n, \tag{31}$$

and $\boldsymbol{I}$ is the identity dyadic.

The tensor $\boldsymbol{\alpha}_p^n$ represent a rotation of the velocity vector due to magnetic field. Even though the second and third terms in the parentheses are higher order terms in Δt, we should not simplify $\boldsymbol{\alpha}_p^n$ further unless the problem is pure electrostatic. We also note that $\boldsymbol{\alpha}_p^n$ is uniquely determined for each particle, not for each species like the classical case [9].

Substituting Eq. (25) into Eq. (18) and keeping only first-order terms in Δt [10], we have

$$\rho_s^{n+1/2}(\boldsymbol{x}) \simeq \rho_s^n(\boldsymbol{x}) - \frac{\Delta t}{2}\nabla \cdot \left(\sum_{p=1}^{Ns} q_p \bar{\boldsymbol{v}}_p W(\boldsymbol{x} - \boldsymbol{x}_p^{n+1/2}) \right), \tag{32}$$

where

$$\rho_s^n(\boldsymbol{x}) = \sum_{p=1}^{Ns} q_p W(\boldsymbol{x} - \boldsymbol{x}_p^n). \tag{33}$$

By the same token, an expression for the time-advanced current density can be obtained by a similar Taylor expansion, keeping only first-order terms in Δt:

$$\boldsymbol{J}_s^{n+1/2}(\boldsymbol{x}) \simeq \widehat{\boldsymbol{J}}_s(\boldsymbol{x}) - \frac{\varepsilon_0}{\theta \Delta t}\boldsymbol{\mu}_s^n \cdot \boldsymbol{E}^{n+\theta} - \frac{\Delta t}{2}\nabla \cdot \widehat{\boldsymbol{\Pi}}_s(\boldsymbol{x}), \tag{34}$$

where

$$\widehat{\boldsymbol{J}}_s(\boldsymbol{x}) = \sum_{p=1}^{Ns} q_p \widehat{\boldsymbol{v}}_p W(\boldsymbol{x} - \boldsymbol{x}_p^n), \tag{35}$$

$$\widehat{\boldsymbol{\Pi}}_s(\boldsymbol{x}) = \sum_{p=1}^{Ns} q_p \widehat{\boldsymbol{v}}_p \widehat{\boldsymbol{v}}_p W(\boldsymbol{x} - \boldsymbol{x}_p^n) \tag{36}$$

and an effective dielectric tensor $\boldsymbol{\mu}_s^n$ is given by

$$\boldsymbol{\mu}_s^n = -\sum_p \frac{q_s \theta \Delta t^2}{2\varepsilon_0 m_s} \boldsymbol{\alpha}_p^n W(\boldsymbol{x} - \boldsymbol{x}_p^n). \tag{37}$$

As we mentioned above, the summation of the effective dielectric tensor $\boldsymbol{\alpha}_p^n$ should be calculated for each particle. Each particle moving with relativistic speed has different effective mass, which affects to $\boldsymbol{\alpha}_p^n$ through its gamma factor.

Lastly, we expand $\bar{\boldsymbol{v}}$ in Eq. (32),

$$\rho_s^{n+1/2} = \rho_s^n - \frac{\Delta t}{2}\nabla \cdot \left(\widehat{\boldsymbol{J}}_s(\boldsymbol{x}) - \frac{\varepsilon_0}{\theta \Delta t}\boldsymbol{\mu}_s^n \cdot \boldsymbol{E}^{n+\theta} - \frac{\Delta t}{2}\nabla \cdot \widehat{\boldsymbol{\Pi}}_s(\boldsymbol{x}) \right). \tag{38}$$

We should note here that the expression in the parentheses of Eq. (38) is the same as Eq. (34), only if the weight function W is the same for the density and current. If this is the case, we can reduce the calculation by substituting the divergence of Eq. (34) into Eq. (38).

Thus, the expansion of the interpolation function W provides a direct and explicit closure of Maxwell's equations Eqs. (34) and (38), and Maxwell's equations can be solved without further iteration with equation of motion. To solve Maxwell's equations, we employ the second-order formulation, which is used in the latest version of CELESTE3D [9].

The curl of Eq. (13) can be written as

$$\nabla \times \nabla \times \boldsymbol{E}^{n+\theta} + \frac{1}{\theta \Delta t} \nabla \times (\boldsymbol{B}^{n+\theta} - \boldsymbol{B}^{n}) = 0. \tag{39}$$

Here we assume that the generic quantity Ψ at time $n+\theta$ are given by linear interpolation, $\Psi^{n+\theta} = \theta \Psi^{n+1} + (1-\theta)\Psi^{n}$. Next, we substitute Eq. (14) into magnetic field terms in Eq. (39), which yields

$$(c\theta\Delta t)^2 \nabla \times \nabla \times \boldsymbol{E}^{n+\theta} + \boldsymbol{E}^{n+\theta} - \boldsymbol{E}^{n} - c^2 \theta \Delta t (\mu_0 \boldsymbol{J}^{n+1/2} - \nabla \times \boldsymbol{B}^{n}) = 0. \tag{40}$$

Next, using the vector identity $\nabla \times \nabla \times \boldsymbol{E} = \nabla(\nabla \cdot \boldsymbol{E}) - \nabla^2 \boldsymbol{E}$ and Poisson's equation Eq. (15), we have

$$(c\theta\Delta t)^2 (-\nabla^2 \boldsymbol{E}^{n+\theta}) + \boldsymbol{E}^{n+\theta} = \boldsymbol{E}^{n} + c^2 \theta \Delta t (\mu_0 \boldsymbol{J}^{n+1/2} - \nabla \times \boldsymbol{B}^{n}) - (c\theta\Delta t)^2 \nabla \frac{\rho^{n+\theta}}{\epsilon_0}. \tag{41}$$

We can separate the terms $\boldsymbol{J}^{n+1/2}$ and $\boldsymbol{\rho}^{n+\theta}$ so that the RHS of Eq.(41) depends only on the variables at $t = n$ and the LHS only on $\boldsymbol{E}^{n+\theta}$ as follows.

From Eqs. (15), (34) and (38), $\boldsymbol{E}^{n+\theta}$ can be written as

$$\nabla \cdot \boldsymbol{E}^{n+\theta} = \frac{\widehat{\rho}}{\varepsilon_0} - \nabla \cdot (\boldsymbol{\mu}^{n} \cdot \boldsymbol{E}^{n+\theta}), \tag{42}$$

where $\widehat{\rho}$ is defined as

$$\widehat{\rho} = \rho^{n} - (\theta \Delta t) \nabla \cdot (\widehat{\boldsymbol{J}} - \frac{\Delta t}{2} \nabla \cdot \widehat{\boldsymbol{\Pi}}). \tag{43}$$

Since $\rho^{n+\theta} = \rho^{n} - \theta \Delta t \nabla \cdot \boldsymbol{J}^{n+1/2}$, $\boldsymbol{E}^{n+\theta}$ can be separated out. The resulted second-order time-discretized equation is given by

$$\begin{aligned} (c\theta\Delta t)^2 [-\nabla^2 \boldsymbol{E}^{n+\theta} - \nabla\nabla \cdot (\boldsymbol{\mu}^{n} \cdot \boldsymbol{E}^{n+\theta})] + \boldsymbol{\epsilon}^{n} \cdot \boldsymbol{E}^{n+\theta} = \\ \boldsymbol{E}^{n} + c^2 \theta \Delta t \left(\mu_0 \widehat{\boldsymbol{J}} - \frac{\Delta t}{2} \nabla \cdot \widehat{\boldsymbol{\Pi}} - \nabla \times \boldsymbol{B}^{n} \right) - (c\theta\Delta t)^2 \nabla \frac{\widehat{\rho}}{\varepsilon_0}, \end{aligned} \tag{44}$$

where $\boldsymbol{\mu}^{n} = \sum_s \boldsymbol{\mu}_s^{n}$ and $\boldsymbol{\epsilon}^{n} = \boldsymbol{I} + \boldsymbol{\mu}^{n}$, where $\boldsymbol{I}$ is the identity tensor.

As shown in Ref. [12], the second order formulation for the electric field needs to be coupled with a divergence cleaning step to ensure that

$$\epsilon_0 \nabla \cdot \boldsymbol{E}^{n} = \rho^{n}, \tag{45}$$

holds for each timestep. Lastly, magnetic field is computed directly from the electric field as

$$\boldsymbol{B}^{n+1} = \boldsymbol{B}^{n} + \Delta t (\nabla \cdot \boldsymbol{E}^{n+\theta}). \tag{46}$$

Using the temporal second-order formulation (44), the field equations are discretized in space using a finite volume approach described in Ref. [14]. The discretized equations and the divergence cleaning along with their boundary conditions are solved using generalized minimal residual algorithm (GMRES) [15]. For the simplicity, we choose the periodic boundary condition in the x direction for our new 1D code.

A Krilov vector of unknowns is defined by three components of the electric field on all interior and boundary nodes, and corresponding residuals are provided by the Maxwell's equation (44) in the interior and the boundary conditions indicated in Ref. [12] on the boundary nodes. GMRES solves this nonsymmetric linear system by minimizing the residual within a prescribed relative tolerance.

B. Particle Mover

After fields are computed, particles can be advanced implicitly. The equations of motion Eqs. (19) and (20) couple with each other. However, the coupling is purely local and does not involve coupling with other particles because of no collision. In previous implementations of the implicit PIC method, a predictor-corrector (PC) approach [13] and the Newton-Krylov (NK) approach [16] are employed to solve the nonlinear system of equations of motions.

The equations of motion for the relativistic particles are Eqs. (19) and (20). First, we show that the energy conserves if electric field $\boldsymbol{E}$ is purely electrostatic ($\boldsymbol{E} = -\nabla\phi$, where ϕ is the scalar potential) with or without magnetic field. Since $\sqrt{1+p^2} = \gamma$, the product of Eq. (20) and $\boldsymbol{p}^{n+1} + \boldsymbol{p}^n$ yields

$$\gamma^{n+1} - \gamma^n = -\nabla\phi \cdot \bar{\boldsymbol{v}}\Delta t. \tag{47}$$

Substituting Eq.(19) into Eq. (47), we have

$$\gamma^{n+1} + \phi^{n+1} = \gamma^n + \phi^n + O(\Delta\boldsymbol{x}^2). \tag{48}$$

Thus, this scheme conserves the energy up to the spatial leading order $\Delta\boldsymbol{x}$. For the PC method, we further assume that Eq. (24) is valid, i.e., the collection term $\Delta\gamma_p$ is small in order to reduce the non-linearity.

As the PC method, we perform the calculation as follows. First, we assume that $\boldsymbol{p}^{n+1} = \boldsymbol{p}^n$ and $\boldsymbol{x}^{n+1} = \boldsymbol{x}^{n+1/2} = \boldsymbol{x}^n$ for each particle. Next, the electric and magnetic field strengths

at the position $\boldsymbol{x}^n$ is calculated by linear interpolation of the field value on nearest grids. The average velocity $\bar{\boldsymbol{v}}$ is calculated using Eq. (25), and then the position $\boldsymbol{x}^{n+1/2}$ is updated using Eq. (19). Now we can perform the second iteration using the new position $\boldsymbol{x}^{n+1/2}$. In our code, we perform this cycle three times to let the solution converge.

There are two problems with the PC method. One is we do not know how much error, including the approximation in Eq. (24), in velocity and position is involved after three iterations. The other is there is no restriction for the new velocity to be less than the speed of light. In relativistic calculation, the second problem can be critical, since we need to have γ factor of each particle at each timestep.

To resolve these problems, we employ the NK method which solves the equations of motions Eqs. (19) and (20) directly without any assumptions. Substituting Eq. (21) into Eq.(20) yields the nonlinear function expressing the discretized Newton equation as

$$\boldsymbol{f}(\boldsymbol{u}_p^{n+1}) = \frac{\boldsymbol{u}_p^{n+1} - \boldsymbol{u}_p^n}{\Delta t} - \frac{q_s}{m_s}\left(\widehat{\boldsymbol{E}}_p^{n+\theta}(\boldsymbol{x}_p^{n+1/2}) + \frac{\boldsymbol{u}_p^{n+1} + \boldsymbol{u}_p^n}{\gamma_p^{n+1} + \gamma_p^n} \times \boldsymbol{B}_p^n(\boldsymbol{x}_p^{n+1/2})\right). \tag{49}$$

Here, only the components of $\boldsymbol{u}_p^{n+1}$ are unknown, with all the other quantities known.

The residual equation $\boldsymbol{f}(\boldsymbol{u}_p^{n+1}) = 0$ is solved using the NK method. The advantage of using the NK method is that the Jacobian matrix never needs to be calculated or formed, and the method uses a series of residual function evaluations [9, 16].

Another advantage for using the NK method is that we ensure the convergence and accuracy of the solution of the equations of motions, whereas the PC method with finite number of iteration allows for an uncontrolled error. We show in Section III that the NK method improves the energy conservation with large timesteps.

We implemented the relativistic movers along with the classical movers with the PC and NK methods [9] for the comparison.

III. NUMERICAL EXAMPLES

We examine the stability of each scheme by performing a number of test simulations in the electrostatic and electromagnetic limits with a wide range of spatial and temporal scales. We use the NK method for all the runs unless otherwise mentioned.

A. The electrostatic limit

In the electrostatic limit, significant deviations from local charge neutrality occur rapidly. Several future of the newly developed 1D code, including energy conservation, numerical stability, difference between particle mover schemes are explored in calculations of the two-stream instability and ion acoustic wave damping.

1. Two Stream Instability

The instability is caused by counter-streaming electrons with $v_0/c = \pm 0.9\widehat{\boldsymbol{x}}$ in the frame of the neutralizing ion background. Ions are immobile in this simulation ($m_e/m_i = 0$) for the simplicity. The simulation box is periodic, and has a physical length $L\omega_{pe}/c = 10$, where $\omega_{pe} = \sqrt{ne^2/(\varepsilon_0 m)}$ is the electron plasma frequency. Initially, the electrons are given the temperature with $V_{the} = 0.001c$. The simulation box has 64 cells of equal size, with 1000 super-particles in each cell. The assumption of the implicit moment method ($v\Delta t/\Delta x < 1$) constrains the maximum allowable time step $\omega_{pe}\Delta t_m \simeq 0.17$. The time-decentering parameter θ is unity. The external magnetostatic field is chosen to be zero.

The dispersion relation for the given wavenumber k and frequency ω is given by

$$2\gamma_0^3 = \omega_{pe}^2 \left[\frac{1}{(kv_0 - \omega)^2} + \frac{1}{(kv_0 + \omega)^2} \right], \tag{50}$$

where $\gamma_0 = 1/\sqrt{1 - v_0^2}$. The system is unstable when the condition $(kv_0)^2\gamma_0^3 < \omega_{pe}^2$ is satisfied. We choose $L\omega_{pe}/c = 10$ so that only the mode with the shortest wavenumber k_{min} is unstable.

Figure 1 shows the growth of the electric field strength associated with the shortest wavenumber E_{kmin}^2. The time-decentering parameter is $\theta = 1$, and $\Delta t\omega_{pe} = 0.01$ in these runs. The system becomes unstable due to the initial thermal distribution. One can observes that both the PC (red line) and NK (green line) methods give the same growth rate of the electric field, which corresponds to the linear growth rate (blue line) given by Eq. (50). The results of the PC and NK methods differ from each other only after the instability fully developed and electric field saturated.

Another set of simulation runs was performed for the case where the system is forced to

be unstable by adding the perturbation

$$x_{new} = x_{old} + 0.01 \times \frac{\cos(k_{min} x_{old})}{k_{min}}, \tag{51}$$

to originally uniformly distributed electrons. We change the time-decentering parameter θ and Δt to compare the error of the total energy and the CPU time for single timestep Δt_{st}. All the runs are performed until they reach the same time $t\omega_{pe} = 200$ in the simulation. For the PC method, we perform runs with 3 and 10 iterations for all the cases, which do not show any fundamental difference. We show here the results with 3 iterations only.

Shown in Table I is the standard deviation σ of total energy $E_{tot}(t)$ and Δt_{st} for $\theta = 0.5, 1$ and $\delta t = 0.1, 0.01$, with the PC and NK methods. The standard deviation σ is defined as

$$\sigma = \sqrt{\frac{1}{N} \sum_{t=0}^{N} \left(\frac{E_{tot}(t) - E_{tot}(0)}{E_{tot}(0)} \right)^2}. \tag{52}$$

The results with the PC method generally has larger total energy error than the NK method, but with shorter calculation time, as we expected. In general, $\theta = 1$ conserves energy better than 0.5 with the PC method, because electron plasma wave is always damped when $\theta = 1$, and energy loss by the wave damping compensates with the increase of particle energy by the PC method. However, opposite is true with the NK method since the particle energy conserves better than the PC method, requiring no wave damping in the Maxwell's equation solver.

We also perform the cases $\omega_{pe}\Delta t > \omega_{pe}\Delta t_m = 0.17$ only for the purpose if the implicit method converges with timesteps larger than allowed. The NK method conserves energy well even Δt exceeds the limit $\Delta t = 0.2$, whereas the conservation becomes much worse with the PC method.

2. Ion Acoustic Wave Damping

In the previous TSI runs, ions are immobile meaning the simulation is essentially explicit and the movement of electrons needs to be resolved by taking short ($\simeq 1/\omega_{pe}$) timestep. In the IAW runs, we change the ion-electron mass ratio m_i/m_e from 25 to 1837 with larger ($\simeq 1/\omega_{pi}$) timestep.

Ion acoustic wave with phase velocity c_s lying between V_{thi} and V_{the} damps slowly because of the weak Landau damping of waves due to ions and electrons. The dispersion relation of

the ion acoustic wave of Hydrogen in the classical limit is given by [17]

$$2k^2\lambda_D^2 = Z'\left(\frac{\omega}{\sqrt{2}kV_{the}}\right) + \frac{T_e}{T_i}Z'\left(\frac{\omega}{\sqrt{2}kV_{thi}}\right), \tag{53}$$

where Z is the plasma dispersion function, $\lambda_D = \sqrt{\varepsilon_0 KT_e/(ne^2)}$ is the Debye length, and prime denotes the first derivative. We solve the dispersion relation (53) numerically to determine the damping rate $Im(\omega)$. The simulation box is periodic, and has a physical length $L\omega_{pe}/c = 5$. Since smaller wavenumber has a smaller damping rate, we perturb the smallest wavenumber mode by perturbing the distribution of charge instead of position,

$$q_{new} = q_{old} + 0.01 \times \frac{\cos(k_{min}x_{old})}{k_{min}}, \tag{54}$$

and compare the damping rate with the linear calculation.

In the first set of runs, we fix the ion-electron mass ratio as $m_i/m_e = 25$, and choose the ion temperature $V_{thi} = 0.01c$ with the electron temperature $V_{the} = 0.3c$ and $0.9c$ in order to compare the classical and relativistic calculations. The simulation box of length $L = 5c/\omega_{pi}$ has 32 cells of equal size, with 1000 super-particles in each cell. The constraint $V_{the}\Delta t/\Delta x < 1$ gives the maximum allowable time step $\omega_{pi}\Delta t_m \simeq 0.52$ and 0.174 for $V_{the} = 0.3c$ and $0.9c$, respectively. We choose $\omega_{pi}\Delta t = 0.1$ to satisfy the constraints.

Figure 2 shows the damping of electric field strength associated with the smallest wave number $E^2_{x,kmin}$ with $V_{the} = 0.3c$. The results by PC and NK methods are identical, and we show the NK method results here. The results with the classical particle mover (red line) and the relativistic mover (green line) methods agree with the linear damping rate (blue line) up to the frequency.

Figure 3 shows the result of the run with $V_{the} = 0.9c$, $\theta = 1$. The damping rate and frequency of the mode with the classical particle mover (solid red line) match with the linear analysis (dotted blue line) in the early phase of the simulation ($t\omega_{pi} \sim 40$), but the damping rate becomes smaller because of the non-linear interaction with other wavenumber modes. The relativistic particle mover (dashed green line) damps similar to the classical case, but the frequency is much lower, because the plasma frequency for energetic electrons becomes lower as

$$\omega_{pe} = \frac{\omega_{pe0}}{\sqrt{\gamma}}, \tag{55}$$

where ω_{pe0} is the classical plasma frequency. We plot the linear damping rate (fine dotted magenta line) with relativistic correction $\omega/\sqrt{\gamma}$ with $\gamma = 1/\sqrt{1-0.9^2}$, which is closer to

the relativistic run.

In the second set of runs, we fix $V_{thi} = 0.01c$, $\theta = 1$, $\omega_{pi}\Delta t = 0.3$, and change the mass ratio $M/m = 100$ and 1837. The simulation box of length $L = 5c/\omega_{pi}$ has 32 cells of equal size. For the run with $M/m = 100$, we choose $V_{the} = 0.3c$ with 5000 super-particles in each cell , and for the run with $M/m = 1837$, $V_{the} = 0.4c$ with 10000 super-particles in each cell. The number of particles per cell is increased from the run with $M/m = 25$ in order to suppress numerical instability. We perform all the runs with the relativistic particle mover other than the last case, and compare the results between the PC and NK methods.

Figure 4 shows the damping of electric field strength associated with the smallest wave number $E^2_{x,kmin}$ with $M/m = 100$. The frequency and damping rate of both runs are quite close to the linear analysis (dotted blue line), yet the NK method (dash green line) gives the better damping rate than the PC method (solid red line). The NK method also conserves the total energy better with $\sigma = 7.1 \times 10^{-3}$, whereas $\sigma = 2.5 \times 10^{-2}$ with the PC method.

Figure 5 shows the damping of electric field strength associated with the smallest wave number $E^2_{x,kmin}$ with $M/m = 1837$. The frequency and damping rate of runs with the classical PC method (solid red line) and the relativistic NK method (dash green line) are quite close to the linear analysis (dotted blue line). In both cases, the damping rate is so fast that non-linear interaction between other modes dominates. We note here that the relativistic PC method fails after four timesteps because the predicted velocity of electrons exceeds the speed of light, as we mentioned in Sec. II B. Even though the initial temperature is low, it is essential to solve the relativistic equations of motion Eqs. (19), (20) instead of classical ones.

B. The electromagnetic limit

In the electromagnetic limit, the gyro-motion of particles by the existence of magnetic filed needs to be solved. It is essential to include magnetic field terms in the Maxwell's equation source terms ρ and $\boldsymbol{J}$ through the dielectric tensor Eq. (37), even though these terms are higher order terms in Δt. Relativistic future of the code in the electromagnetic limit is explored in calculations of the Weibel instability and Poynting flux acceleration.

1. The Weibel Instability

We examine the Weibel instability in a relativistic bi-Maxwellian plasma [18]. The anisotropy of electron phase distribution drives the Weibel instability even in one-dimensional plasma.

In this simulation we fix ions as a uniform background ($m_e/m_i = 0$) for the simplicity. The initial electron distribution function is given as

$$f_e(p_\perp^2, p_\parallel) = \frac{\alpha_\perp}{4\pi(m_e c)^3 K_2(\alpha_\parallel)} \frac{\exp[-\alpha_\perp(\gamma - \gamma_\parallel) - \alpha_\parallel \gamma_\parallel]}{1 + (\alpha_\parallel/\alpha_\perp - 1)[K_1(\alpha_\parallel)/\{\alpha_\parallel K_2(\alpha_\parallel)\}]}, \tag{56}$$

where

$$\gamma = \left(1 + \frac{p_\perp^2}{m_e^2 c^2} + \frac{p_\parallel^2}{m_e^2 c^2}\right)^{1/2}, \quad \gamma_\parallel = \left(1 + + \frac{p_\parallel^2}{m_e^2 c^2}\right)^{1/2}. \tag{57}$$

Here $K_n(x)$ is a modified Bessel function of the second kind of order n, and the subscripts perpendicular and parallel refer to the directions perpendicular and parallel to the wave vector $\boldsymbol{k}$, whose direction is parallel to the x direction of the simulation box, respectively. The parameters $\alpha_\perp$ and $\alpha_\parallel$ both range from 0 (ultrarelativistic limit) to ∞ (nonrelativistic limit). The distribution function (56) reduces to the nonrelativistic bi-Maxwellian distribution

$$f_e(p_\perp^2, p_\parallel) = \frac{\exp[-p_\perp^2/(2m_e T_\perp) - p_\parallel^2/(2m_e T_\parallel)]}{2\pi m_e T_\perp \sqrt{2\pi m_e T_\parallel}}, \tag{58}$$

in the limit $\alpha_\perp \gg 1$ and $\alpha_\parallel \gg 1$.

The relationship between the parameters $\alpha_\perp$ and $\alpha_\parallel$ and the effective perpendicular and parallel temperatures $T_\perp$ and $T_\parallel$ are defined as follows:

$$\frac{T_\perp}{m_e c^2} = \frac{1}{\alpha_\perp}, \tag{59}$$

$$\frac{T_\parallel}{m_e c^2} = \frac{1}{\alpha_\parallel}\left[\left(\frac{\alpha_\parallel}{\alpha_\perp} - 1\right)\frac{K_1(\alpha_\parallel)}{\alpha_\perp K_2(\alpha_\parallel)}\right]^{-1}. \tag{60}$$

The instability condition is given by (see [18] for detailed calculations)

$$T_\perp/T_\parallel > 1. \tag{61}$$

When $T_\perp > T_\parallel$, the approximate growth rate γ_k of the unstable Weibel mode is given by

$$\frac{\gamma_k^2}{\omega_{pe}^2} = \frac{k^2}{k_0^2}\left(1 - \frac{k^2}{k_0^2}\right)^2 \frac{T_\parallel}{m_e c^2}\left(\frac{T_\perp}{T_\parallel} - 1\right)^3 \left(\frac{\alpha_\perp K_2(\alpha_\parallel) + K_0(\alpha_\parallel)}{\alpha_\perp K_2(\alpha_\parallel) + K_1(\alpha_\parallel)}\right)^3 \left(\frac{1}{K_2(\alpha_\parallel)}\int_0^\infty d\tau \frac{K_2(\alpha_\parallel \xi')}{\xi'^2}\right)^{-2}, \tag{62}$$

where $\xi'^2 = 1 + \tau^2$, and the maximum wave number k_0 is given by

$$k_0^2 = \frac{\omega_{pe}^2}{c^2}\left(\frac{\alpha_\parallel}{\alpha_\perp} - 1\right)\left(\frac{K_1(\alpha_\parallel)}{K_2(\alpha_\parallel)} + \frac{K_0(\alpha_\parallel)}{\alpha_\perp K_2(\alpha_\parallel)}\right)\left[1 + \left(\frac{\alpha_\parallel}{\alpha_\perp} - 1\right)\frac{K_1(\alpha_\parallel)}{\alpha_\parallel K_2(\alpha_\parallel)}\right]^{-1}. \quad (63)$$

Note that the wavenumber associated with the maximum growth rate is given by $k_{max}^2 = k_0^2/3$.

Following Yoon [18], we fix the rate $\alpha_\parallel/\alpha_\perp - 1 = 0.1$, and choose the electron temperature $\alpha_\perp = m_e c^2/T_\perp = 1$ and 10. The simulation box of length $L = 2\pi/k_{max}$ has 64 cells of equal size, with 2000 super-particles in each cell. We use the relativistic NK method particle mover, because of the relativistic initial temperature. We choose $\Delta t\omega_{pe} = 0.1$, which does not exceed the implicit constraints.

The result is shown in Fig. 6. Solid red line indicates the magnetic field strength $B_{y,max}^2$ with $\alpha_\perp = 1$, and the dashed green line with $\alpha_\perp = 10$. Dotted blue and fine dotted magenta lines indicate the linear growth rate $\gamma_k = 0.0236\omega_{pe}$ for the case $\alpha_\perp = 1$, and $\gamma_k = 0.013\omega_{pe}$, for $\alpha_\perp = 10$, respectively. It is clear, especially with ultra-relativistic temperature ($\alpha_\perp = 1$), that the magnetic field B_y grows linearly with the growth rate calculated from the linear theory.

2. Poynting Flux Acceleration

Lastly, we examine the code against the Poynting flux acceleration (PFA) [19–21]. The electron-positron plasma embedded in linearly polarized uniform magnetic field is accelerated due to Ponderomotive force. We compare results of the implicit code with the explicit code [21].

In this run, we fix the positron-electron mass ratio as unity, and choose the electron and positron temperature as $V_{the} = V_{thp} = 1$ MeV. The simulation box of length $L = 51.2c/\omega_{pe}$ has 512 cells of equal size, with 12800 super-particles. We choose initial uniform magnetic field strength B_{y0} as $B_{y0}^2 = 100nm_e/\varepsilon_0$ so that $\Omega_{ce}/\omega_{pe} = 10$. We choose $\Omega_{ce}\Delta t = 0.2$ in order to resolve gyro-motion in the explicit run, and $\theta = 1$.

Initially, particles are uniformly distributed in thin slab $-0.5c/\omega_{pe} < x < 0.5c/\omega_{pe}$ at the center of the box, where initial uniform magnetic field $\boldsymbol{B}_0 = (0, B_{y0}, 0)$ is also applied. As magnetic field B_y expands to the positive and negative x directions, electric field E_z is generated. Next, particles are accelerated by the $\boldsymbol{E} \times \boldsymbol{B}$ force in the direction of Poynting

vector. Since electromagnetic wave moves with nearly the speed of light, only energetic particles comoving with the wave continuously get accelerated, leaving slow particles behind of the wave.

Figure 7 shows the phase plot of particles at $t\Omega_{ce} = 0$ (red), 400 (green) and 1000 (blue). Since particle expansion is symmetric, we show the result of the explicit code in $x < 0$, and the implicit code in $x > 0$. The most energetic particles reach $p_x = 60 m_e c$ at $t\Omega_{ce} = 1000$ in both runs, and the distribution of particles is quantitatively the same. There is no charge separation between electrons and positrons, and the acceleration for high energy particles continues.

Figure 8 shows the profiles of electric field E_z ($x < 0$) and magnetic field ($x > 0$). Red line shows the fields at $t\Omega_{ce} = 0$, dashed green and fine dashed magenta lines show fields from the explicit code and implicit code at $t\Omega_{ce} = 400$, and dotted blue and fine dash-dot cyan lines show fields from the explicit code and implicit code at $t\Omega_{ce} = 1000$, respectively. The front and peak positions and strength of electro-magnetic wave are quite similar to each other at any time. It is remarkably different, though, that the oscillation amplitude in the tail of wave is smaller in the implicit case than in the explicit case. The particle acceleration, however, occurs mainly in the front of electromagnetic wave, and so this difference does not affect to the energetic particle distribution in Fig. 7.

IV. CONCLUSION

In the present paper we have proposed new schemes for the relativistic particle mover and the Maxwell's equations solver, and we presented the newly developed 1D code with its benchmarks. We checked the code against four different problems, TSI (electrostatic, $M/m = \infty$), IAW (electrostatic, $M/m = 1837$), Weibel (electromagnetic, $M/m = \infty$), PFA (electromagnetic, $M/m = 1$).

The former two problems are purely electrostatic. With the TSI runs, we check the performance of the PC and NK methods. In general, the NK method is two times slower than the PC method, but the total energy can be conserved with error less than one percent, with all the particles moving relativistically.

With IAW runs, we perform the full implicit calculation by taking large timestep. It is remarkable that the code is stable with $M/m = 1837$. Since $\omega_{pe}/\omega_{pi} = \sqrt{M/m} \simeq 42.86$

in this case, the equation of motion for electrons are solved fully implicitly ($\Delta t\omega_{pe} = 12.9$). Even though this specific run needs 50 times more super-particles per cell for the stable calculation, it is far much faster than the explicit code, which needs to resolve the electron plasma frequency. We can stabilize the numerical instability further by smoothing field spatially, which is implemented in CELESTE3D [12] and our new code, but the stability analysis of the smoothing effect is beyond the scope of the present paper.

The latter two problems are electromagnetic and fully relativistic. In the Weibel instability case, we observe the exponential growth of magnetic field, which indicates that the magnetic field is correctly coupled with current and electric field, as we expected. We directly compare the result of the implicit code with the explicit code with the PFA case. Phase plots of superparticles from these two codes are almost identical, and field expanding into vacuum has quite similar shapes. Small scale structures of electromagnetic field are averaged out because we solve Maxwell's equations with first-order accuracy in Δt. We tried to run the implicit code with $\theta = 0.5$, but the field solver immediately becomes numerically unstable.

The new relativistic implicit PIC code we proposed here generalized the previous classical implicit schemes, and can be applied to high energy astronomical phenomena and laboratory experiences with multiple space and time scale.

Acknowledgments

The authors thank Jerry Brackbill and Edison Liang for stimulating discussions. The present work is supported by NASA Grant No. NAG5-9223, NSF Grant No. AST0406882, and by the LDRD program at the Los Alamos National Laboratory. Work performed under the auspices of the National Nuclear Security Administration of the U.S. Department of Energy by the Los Alamos National Laboratory, operated by Los Alamos National Security LLC under contract DE-AC52-06NA25396.

---

[1] A. S. S. Lipatov, *The Hybrid Multiscale Simulation Technology* (Springer, Berlin, 2002).

[2] D. Krauss-Varban and N. Omidi, Geophys. Res. Lett. **22**, 3271 (1995).

[3] W. Lee, J. Comp. Phys. **72**, 243 (1987).

[4] Z. Lin, T. S. Hahm, W. W. Lee, W. M. Tang, and R. B. White, Science **281**, 1835 (1998).

[5] G. Lapenta and J. Brackbill, Geophys. Res. Lett. **23**, 1713 (1996).

[6] W. Daughton, G. Lapenta, and P. Ricci, Phys. Rev. Lett. **93**, 105004 (2004).

[7] J. F. Drake, M. Swisdak, C. Cattell, M. A. Shay, B. N. Rogers, and A. Zeiler, Science **299**, 873 (2003).

[8] C. Birdsall and A. Langdon, *Plasma Physics Via Computer Simulation* (Taylor & Francis, London, 2004).

[9] G. Lapenta, J. Brackbill and P. Ricci, Phys. Plasmas **13**, 055904 (2006).

[10] H. X. Vu and J. U. Brackbill, Comp. Phys. Comm. **69**, 253 (1992).

[11] J. Brackbill and D. Forslund, J. Comp. Phys. **46**, 271 (1982).

[12] P. Ricci, G. Lapenta, and J. Brackbill, J. Computat. Phys. **183**, 117 (2002).

[13] H. Vu and J. Brackbill, J. Comp. Phys. **116**, 384 (1995).

[14] D. Sulsky and J. U. Brackbill, J. Comp. Phys. **96**, 339 (1991).

[15] Y. Saad, *Iteractive Methods for Sparse Linear Systems* (SIAM, Philadelphia, 2003).

[16] C. T. Kelley, *Iterative methods for linear and nonlinear equations* (SIAM, Philadelphia, 1995).

[17] T. J. M. Boyd and J. J. Sanderson, *The Physics of Plasmas* (Cambridge, Cambridge, 2003).

[18] P. H. Yoon, Phys. Fluids B **1**, 1336 (1989).

[19] E. Liang, K. Nishimura, H. Li and S. P. Gary, Phys. Rev. Lett. **90**, 085001 (2003)

[20] E. Liang and K. Nishimura, Phys. Rev. Lett. **92**, 175005 (2004)

[21] K. Noguchi, E. Liang and K. Nishimura, Nuovo Ciment C **28**, 381 (2005)

Figure and Table Captions

Figure 1: Growth of electric field strength E^2_{kmin}. Results with the PC method (solid red line) and the NK method (dashed green line) are indicated. Dotted blue line indicates the linear growth rate calculated from Eq. (50).

Figure 2: Damping of electric field strength $E^2_{x,kmin}$ with $V_{the} = 0.3c$. Results with the classical particle mover (solid red line) and the relativistic mover (dashed green line) are indicated. Dotted blue line indicates the linear damping rate $\omega/\omega pi = 7.56 \times 10^{-2} - 8.44 \times 10^{-3} I$, calculated from Eq. (51).

Figure 3: Damping of electric field strength $E^2_{x,kmin}$ with $V_{the} = 0.9c$. Results with the classical particle mover (solid red line) and the relativistic mover (dashed green line) are indicated. Dotted blue line and fine dotted magenta line indicate the linear damping rate $\omega/\omega_{pi} = 2.17 \times 10^{-1} - 2.43 \times 10^{-2} I$, calculated from Eq. (51), and $\omega/\sqrt{\gamma}$.

Figure 4: Damping of electric field strength $E^2_{x,kmin}$ with $M/m = 100$. Results with the classical particle mover (solid red line) and the relativistic mover (dashed green line) are indicated. Dotted blue line indicates the linear damping rate $\omega/\omega_{pi} = 4.32 \times 10^{-2} - 3.95 \times 10^{-3} I$, calculated from Eq. (51).

Figure 5: Damping of electric field strength $E^2_{x,kmin}$ with $M/m = 1837$. Results with the classical particle mover (solid red line) and the relativistic mover (dashed green line) are indicated. Dotted blue line indicates the linear damping rate $\omega/\omega_{pi} = 2.10 \times 10^{-2} - 1.48 \times 10^{-2} I$, calculated from Eq. (51).

Figure 6: Damping of magnetic field strength $B^2_{y,kmax}$ with $\alpha_\perp = 1$ (solid red line)and 10 (dashed green line). Dotted blue and fine dotted magenta lines indicate the linear growth rates $\gamma_k/\omega_{pe} = 2.35 \times 10^{-2}$ for the case $\alpha_\perp = 1$, and $\gamma_k/\omega_{pe} = 1.31 \times 10^{-2}$ for $\alpha_\perp = 10$, respectively.

Figure 7: The phase plot of particles at $t\Omega_{ce} = 0$ (red), 400 (green), and 1000 (blue). Since particle expansion is symmetric, we show the result of the explicit code in $x < 0$, and the implicit code in $x > 0$.

Figure 8: The profiles of electric field E_z ($x < 0$) and magnetic field ($x > 0$). Red line shows the fields at $t\Omega_{ce} = 0$, dashed green and fine dashed magenta lines show fields from the explicit code and implicit code at $t\Omega_{ce} = 400$, and dotted blue and fine dash-dot cyan lines show fields from the explicit code and implicit code at $t\Omega_{ce} = 1000$, respectively.

Table I: Energy error deviation σ and average CPU time per cycle Δt_{st}(s) for the PC and NK particle solvers with $\theta = 0.5$ and 1. The total time considered here is $t\omega_{pe} = 200$.

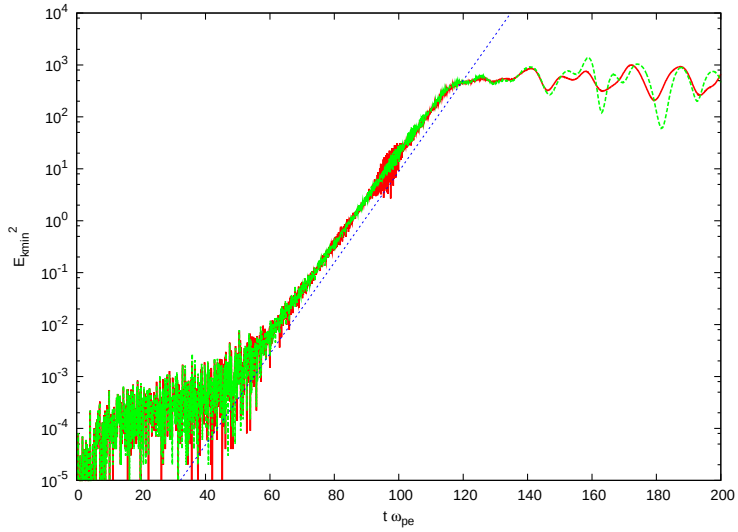

FIG. 1: Growth of electric field strength E^2_{kmin}. Results with the PC method (solid red line) and the NK method (dashed green line) are indicated. Dotted blue line indicates the linear growth rate calculated from Eq. (50).

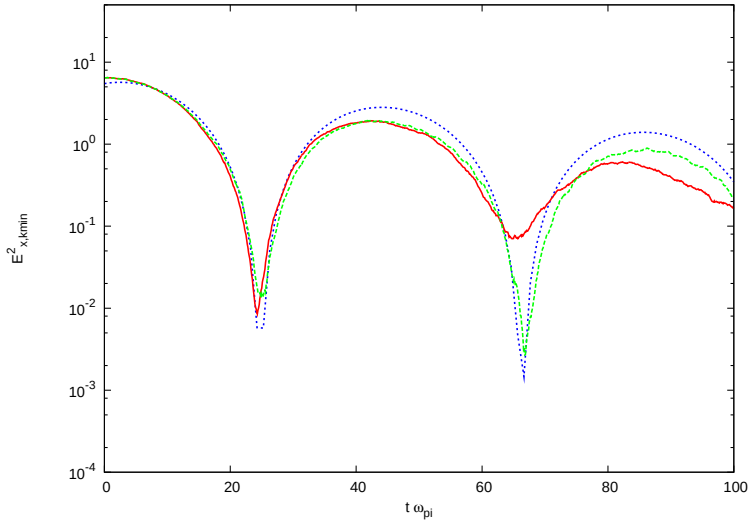

FIG. 2: Damping of electric field strength $E^2_{x,kmin}$ with $V_{the} = 0.3c$. Results with the classical particle mover (solid red line) and the relativistic mover (dashed green line) are indicated. Dotted blue line indicates the linear damping rate $\omega/\omega pi = 7.56 \times 10^{-2} - 8.44 \times 10^{-3} I$, calculated from Eq. (51).

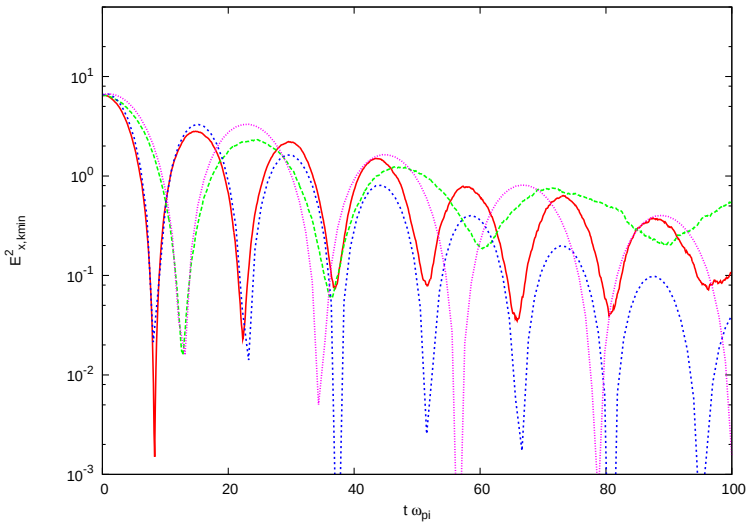

FIG. 3: Damping of electric field strength $E^2_{x,kmin}$ with $V_{the} = 0.9c$. Results with the classical particle mover (solid red line) and the relativistic mover (dashed green line) are indicated. Dotted blue line and fine dotted magenta line indicate the linear damping rate $\omega/\omega_{pi} = 2.17 \times 10^{-1} - 2.43 \times 10^{-2} I$, calculated from Eq. (51), and $\omega/\sqrt{\gamma}$.

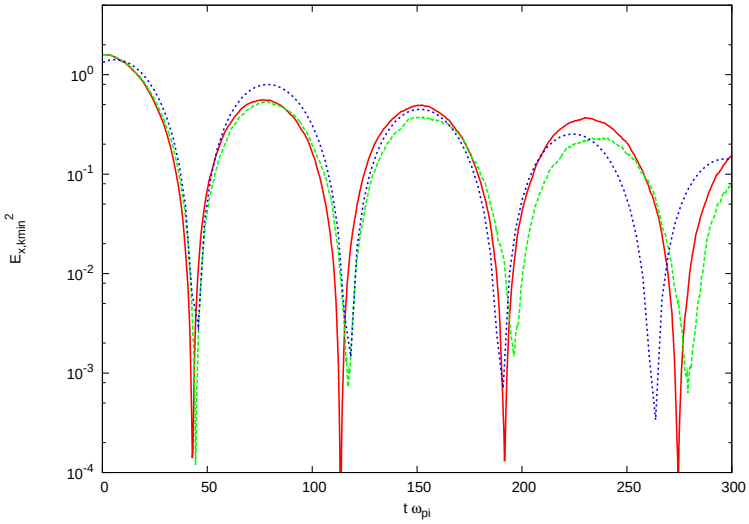

FIG. 4: Damping of electric field strength $E^2_{x,kmin}$ with $M/m = 100$. Results with the classical particle mover (solid red line) and the relativistic mover (dashed green line) are indicated. Dotted blue line indicates the linear damping rate $\omega/\omega_{pi} = 4.32 \times 10^{-2} - 3.95 \times 10^{-3} I$, calculated from Eq. (51).

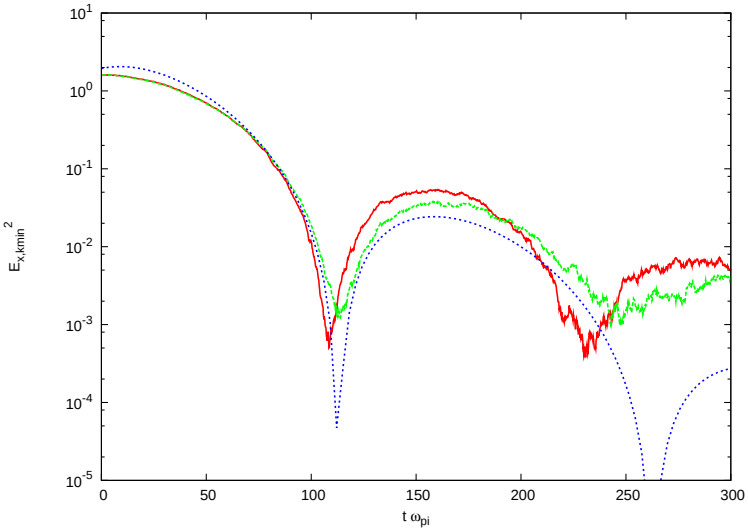

FIG. 5: Damping of electric field strength $E^2_{x,kmin}$ with $M/m = 1837$. Results with the classical particle mover (solid red line) and the relativistic mover (dashed green line) are indicated. Dotted blue line indicates the linear damping rate $\omega/\omega_{pi} = 2.10 \times 10^{-2} - 1.48 \times 10^{-2} I$, calculated from Eq. (51).

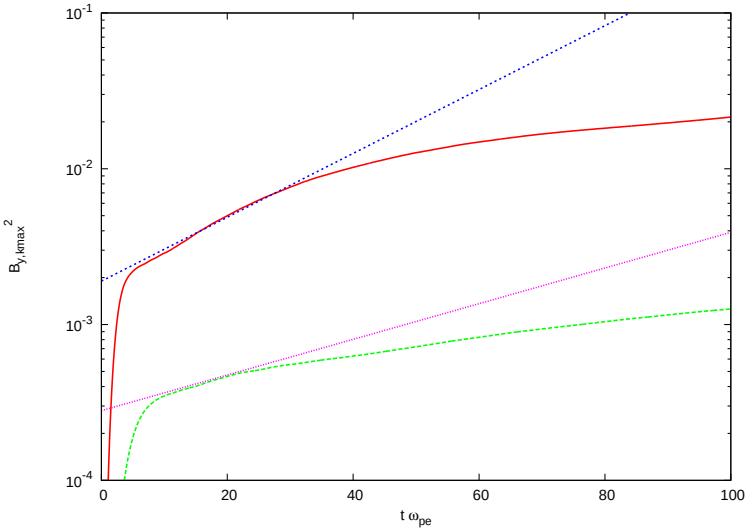

FIG. 6: Damping of magnetic field strength $B^2_{y,kmax}$ with $\alpha_\perp = 1$ (solid red line)and 10 (dashed green line). Dotted blue and fine dotted magenta lines indicate the linear growth rates $\gamma_k/\omega_{pe} = 2.35 \times 10^{-2}$ for the case $\alpha_\perp = 1$, and $\gamma_k/\omega_{pe} = 1.31 \times 10^{-2}$ for $\alpha_\perp = 10$, respectively.

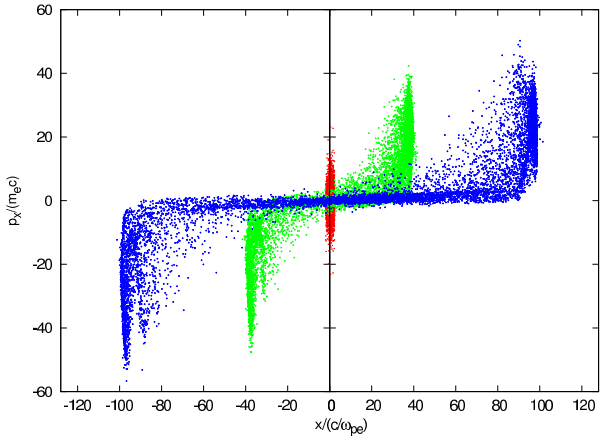

FIG. 7: The phase plot of particles at $t\Omega_{ce} = 0$ (red), 400 (green), and 1000 (blue). Since particle expansion is symmetric, we show the result of the explicit code in $x < 0$, and the implicit code in $x > 0$.

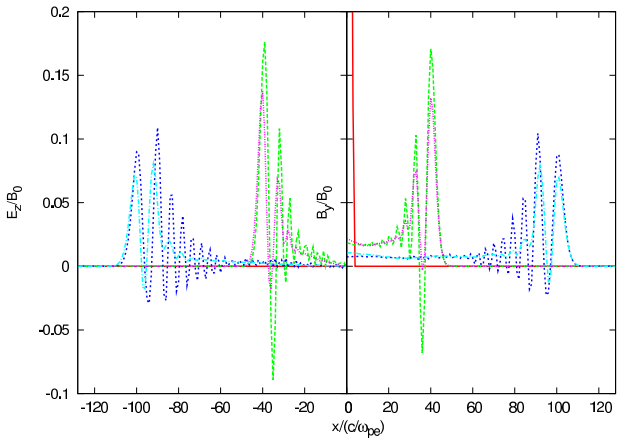

FIG. 8: The profiles of electric field E_z ($x < 0$) and magnetic field ($x > 0$). Red line shows the fields at $t\Omega_{ce} = 0$, dashed green and fine dashed magenta lines show fields from the explicit code and implicit code at $t\Omega_{ce} = 400$, and dotted blue and fine dash-dot cyan lines show fields from the explicit code and implicit code at $t\Omega_{ce} = 1000$, respectively.

TABLE I: Energy error deviation σ and average CPU time per cycle Δt_{st}(s) for the PC and NK particle solvers with $\theta = 0.5$ and 1. The total time considered here is $t\omega_{pe} = 200$.

	Predictor-Corrector				Newton-Krylov			
	$\theta = 0.5$		1		0.5		1	
$\omega_{pe}\Delta t$	σ	Δt_{st}	σ	Δt_{st}	σ	Δt_{st}	σ	Δt_{st}
0.01	5.68×10^{-3}	0.26	4.61×10^{-3}	0.23	1.16×10^{-3}	0.46	2.13×10^{-3}	0.47
0.1	8.55×10^{-2}	0.24	2.65×10^{-2}	0.27	2.82×10^{-3}	0.48	4.65×10^{-2}	0.43
0.17	1.46×10^{-1}	0.27	7.64×10^{-3}	0.29	3.58×10^{-3}	0.53	2.00×10^{-2}	0.48
0.2	1.73×10^{-1}	0.37	2.39×10^{-1}	0.39	4.91×10^{-3}	0.73	7.09×10^{-2}	0.71
1	3.07×10^{-0}	0.89	1.92×10^{-1}	0.52	2.42×10^{-1}	1.08	3.49×10^{-1}	1.12